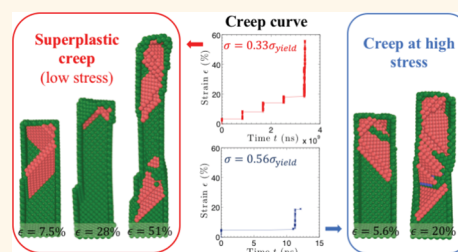


# Superplastic Creep of Metal Nanowires from Rate-Dependent Plasticity Transition

Weiwei Tao,<sup>†</sup> Penghui Cao,<sup>‡</sup> and Harold S. Park<sup>\*,†</sup> <sup>†</sup>Department of Mechanical Engineering, Boston University, Boston, Massachusetts 02215, United States<sup>‡</sup>Department of Nuclear Science and Engineering, Massachusetts Institute of Technology, Cambridge, Massachusetts 02139, United States Supporting Information

**ABSTRACT:** Understanding the time-dependent mechanical behavior of nanomaterials such as nanowires is essential to predict their reliability in nanomechanical devices. This understanding is typically obtained using creep tests, which are the most fundamental loading mechanism by which the time-dependent deformation of materials is characterized. However, due to existing challenges facing both experimentalists and theorists, the time-dependent mechanical response of nanowires is not well-understood. Here, we use atomistic simulations that can access experimental time scales to examine the creep of single-crystal face-centered cubic metal (Cu, Ag, Pt) nanowires. We report that both Cu and Ag nanowires show significantly increased ductility and superplasticity under low creep stresses, where the superplasticity is driven by a rate-dependent transition in defect nucleation from twinning to trailing partial dislocations at the micro- or millisecond time scale. The transition in the deformation mechanism also governs a corresponding transition in the stress-dependent creep time at the microsecond (Ag) and millisecond (Cu) time scales. Overall, this work demonstrates the necessity of accessing time scales that far exceed those seen in conventional atomistic modeling for accurate insights into the time-dependent mechanical behavior and properties of nanomaterials.

**KEYWORDS:** nanowire, superplasticity, creep, rate-dependent deformation, self-learning metabasin escape algorithm



Understanding the time-dependent deformation and failure mechanisms of metallic nanowires is essential for their applications in nanomechanical devices.<sup>1–4</sup>

One important example of this is for stretchable and conductive electronics applications, where the conductivity is strongly dependent on the time-dependent mechanical reliability of the conductive element, the metallic nanowires.<sup>4–7</sup> However, most experimental and computational studies of the mechanical properties and plasticity of metal nanowires have focused on size and microstructure effects.<sup>8–19</sup> In contrast, very few experimental studies have examined the time-dependent deformation of nanowires,<sup>4,20–26</sup> and no experiments we are aware of have examined creep in metal nanowires.

The time-dependent deformation and failure of materials are traditionally assessed *via* creep experiments,<sup>27</sup> where the response of the material to constant applied forces or stresses is monitored. While such creep investigations have previously been performed for nanocrystalline metals,<sup>28–35</sup> they have not for metallic nanowires. The closest such investigation we have found for metal nanowires was the recent experimental and computational study of stress relaxation in single-crystal silver nanowires by Ramachandramoorthy *et al.*<sup>4</sup> and the anelastic relaxation from bending on ZnO and Si nanowires.<sup>20</sup> In the experiments of Ramachandramoorthy *et al.*,<sup>4</sup> the stress–relaxation of the nanowires was examined under constant

strain experimental conditions and also *via* classical molecular dynamics (MD) simulations.

With regards to creep, recent MD simulations of creep in nanocrystalline metals were performed at increased temperature and extremely high creep rates on the order of  $10^7$  s<sup>-1</sup>.<sup>33,34</sup> However, MD simulations suffer from well-known drawbacks, in particular, short accessible time scales and artificially large strain rates,<sup>36,37</sup> and it is thus debatable whether MD simulation results can directly be extrapolated to laboratory conditions.<sup>32</sup> Furthermore, because MD simulations cannot access experimental time scales, direct atomistic observation of rate-dependent plasticity transitions, which have previously been predicted in face-centered cubic (fcc) metals,<sup>38</sup> has not occurred. Therefore, a fundamental and unresolved question that arises and that we attempt to address in this work is what are the mechanisms governing the creep response of single-crystal metal nanowires?

Here, we utilize the recently developed self-learning metabasin escape (SLME) method<sup>39,40</sup> to examine the creep behavior of single-crystal fcc metal (Ag, Cu, Pt) nanowires at

Received: March 23, 2018

Accepted: April 30, 2018

Published: April 30, 2018

time scales ranging from nanoseconds to hundreds of seconds. In doing so, we clearly demonstrate the effects of stress on the evolution of plasticity and thus the operant deformation mechanisms governing both steady-state creep and the subsequent transition to failure. In particular, we find that Cu and Ag nanowires exhibit superplasticity for lower creep stresses, which is enabled by a rate-dependent transition in the defect nucleation from twinning to trailing partial dislocations at the micro- (Ag) or millisecond (Cu) time scales. This shows the necessity of accessing experimentally relevant time scales to gain insights into the time-dependent properties of nanomaterials.

## RESULTS AND DISCUSSION

**Creep Curves.** All results in this section were obtained using the SLME method at room temperature, which will enable us to investigate the atomistic mechanisms governing the evolution of creep in the nanowires at various stresses. We note that MD simulations of creep require increased temperatures in order to ensure that plastic events of interest occur during nanosecond time scales.<sup>33,34</sup> However, because we are not time-scale-restricted due to the SLME method, we focus on the fundamental room temperature creep response here.

To benchmark this approach, we first compare and validate the SLME results for creep at high stresses and short time scales against MD simulations, as shown in the [Supporting Information](#). Specifically, [Figure S2](#) shows that the creep times at high stresses ( $>0.5\sigma_y$ , where  $\sigma_y$  is the yield stress) obtained using the SLME method quantitatively match those obtained using classical MD. We note that the creep stresses are normalized by the yield stress  $\sigma_y$ , where the yield stress is calculated from constant strain rate MD simulations at a strain rate of  $10^9 \text{ s}^{-1}$ . The yield stresses of Pt, Cu, and Ag nanowires are 11.4, 6.7, and 5.3 GPa, respectively, as shown in [Figure S1](#). We have also verified that the SLME method gives the same creep mechanisms as MD by showing in [Figure S3](#), [Video S1](#), and [Video S2](#) the atomistic configurations at different strains under a uniaxial stress of  $0.59\sigma_y$ .

The creep curves for the nanowires follow the classical three stages of creep strain evolution, as shown in [Figure 1](#). In the

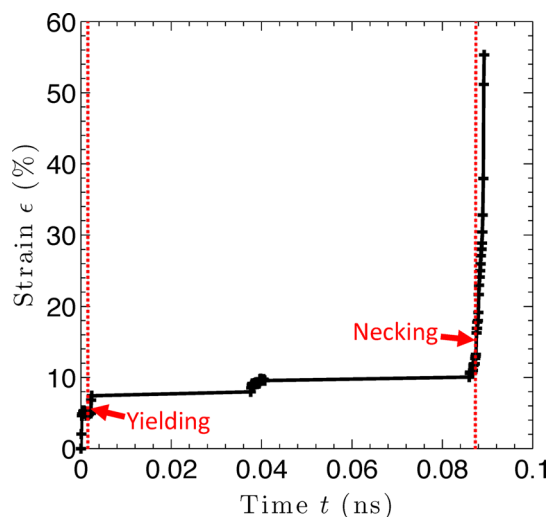


**Figure 1.** Representative creep curve (strain  $\epsilon$  vs time) for a Cu nanowire subject to a creep stress of  $0.59\sigma_y$  at room temperature using the SLME approach.

first stage, a rapid elastic strain generation due to the externally applied constant stress is seen in the first few picoseconds. The secondary stage, or plastic regime, begins with a yield of the nanowire, which occurs *via* the nucleation of dislocations. Different from the steady-state behavior with continuous strain increases with time that is observed in the creep of bulk and nanocrystalline metals due to the existence of internal microstructures and grain boundaries, single-crystal nanowires exhibit periods of discrete strain bursts.<sup>41</sup> As such, none of the conventional grain-boundary-mediated creep processes are operant.<sup>27</sup> Instead, the elongation of the nanowires under the constant stress is entirely governed by the nucleation and interaction of different planar defects. The details of these plastic events and their relationship to the secondary creep time will be discussed later. The third stage begins with the necking of the nanowire, after which the growth of a localized neck leads to failure of the nanowire.

[Figure 2](#) shows a series of creep curves for Cu nanowires until necking for constant applied creep stresses ranging from  $0.33\sigma_y$  to  $0.59\sigma_y$ . The tertiary stage (necking) is not included here as our interest is in the plastic deformation mechanisms in the secondary regime. [Figure 2](#) shows that the applied stress has a significant effect on the time evolution of the creep strain. As the creep stress decreases, the duration of the secondary creep stage increases dramatically, reaching the order of a few seconds for a stress of  $0.33\sigma_y$ . This observation is consistent with the notion that the activation energy for surface dislocation nucleation increases with decreasing tensile stress, and as a result, more time is required for dislocation nucleation as the applied tensile stress decreases.<sup>42</sup> We also observe more discrete strain bursts, which correspond to defect nucleation events, as the stress decreases. The same trend is also observed for Ag and Pt, where [Figures S4 and S5](#) present the creep curves for Ag and Pt across a wide range of creep stresses.

The creep rate, which is the inverse of creep time and is defined as the slope of the creep curve during secondary creep, has been widely used to characterize the creep mechanisms for bulk and nanocrystalline materials. According to the Bird–Dorn–Mukherjee relation,<sup>43</sup> the creep rate  $\dot{\epsilon}$  follows a power-law relationship with stress, which can be expressed as  $\dot{\epsilon} \propto \sigma^n$ , where  $n$  is the stress exponent, which is an important parameter for identifying different creep mechanisms.<sup>33,44</sup> However, these relationships assume that the creep strain is a continuous function of time, which is not the case for the nanowire systems we have considered. Therefore, even though we are not able to determine the creep rate for nanowires, we assume that there is a quantitative relationship between the creep time and stress. By defining the creep time as the time until the onset of necking, we show in [Figure 3](#) the creep time as a function of stress for all three fcc metals (Ag, Cu, Pt). In order to distinguish the curves for different materials, we plot in [Figure 3](#) the actual stress value.

Importantly, for both Ag and Cu nanowires, a decrease in the slope in [Figure 3](#) is observed as the stress decreases. This slope decrement occurs at around 3.2 GPa ( $0.48\sigma_y$ ) for Cu and 2.75 GPa ( $0.52\sigma_y$ ) for Ag. However, no such stress-dependent transition in the slope of the creep stress is observed for Pt nanowires.

**Creep Mechanisms at Different Stresses. High Stress, Short Time Scale Regime.** To uncover the mechanisms that govern the transition in the creep time–stress curve for Ag and Cu shown in [Figure 3](#), we examined the dislocation activity during creep at different stress levels, where all discussions in

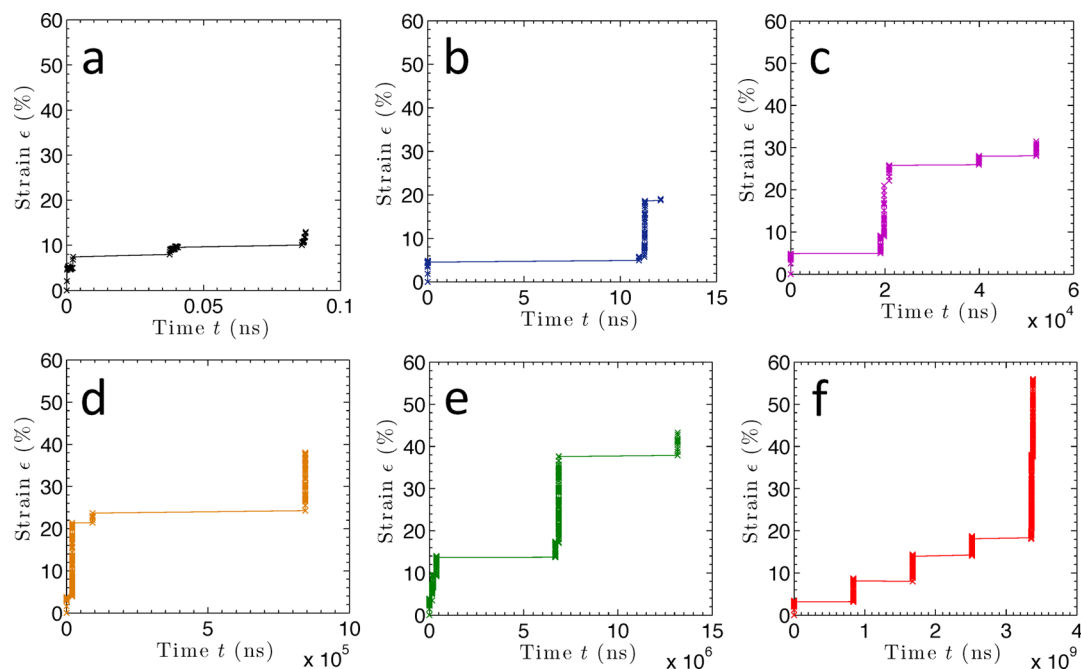


**Figure 2.** SLME simulated creep curves for Cu nanowires at room temperature until the onset of necking for applied creep stresses of (a)  $0.59\sigma_y$ , (b)  $0.56\sigma_y$ , (c)  $0.50\sigma_y$ , (d)  $0.44\sigma_y$ , (e)  $0.38\sigma_y$ , and (f)  $0.33\sigma_y$ .

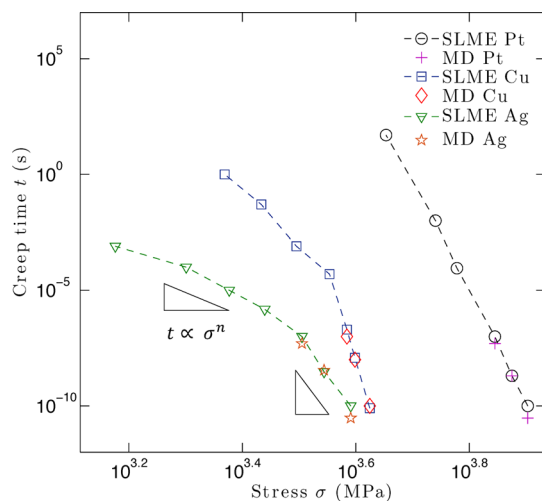


**Figure 3.** Stress dependence of creep time from SLME and MD simulations for Pt, Cu, and Ag.

this section are for the secondary creep stage. Furthermore, because Ag and Cu show similar deformation mechanisms (see Videos S2–S5) that are distinct from those observed in Pt, we will focus our discussions on Cu and Pt for comparison. We first focus on the high stress, short time scale regime, corresponding to creep stresses larger than about  $0.45\sigma_y$ , and creep times shorter than about  $10^{-5}$  s, as shown in Figure 3 for Cu nanowires.

We show in Figure 4 the key deformation mechanisms for high ( $0.56\sigma_y$ ) creep stresses for Cu nanowires. Figure 4a shows that the secondary creep stage starts with the emission of the first leading partial dislocation from an edge of the nanowire on  $\{111\}$  slip planes. The partial dislocation glides through the cross section and intersects with the free surfaces, leaving an intrinsic stacking fault (SF). After emission of the first partial dislocation, the second event can be one of several possible

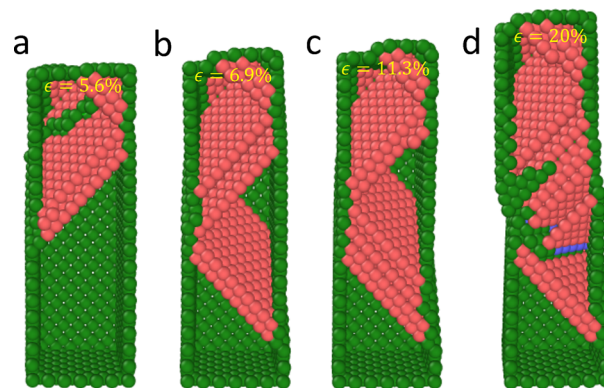


**Figure 4.** Selected atomic configurations during the creep deformation of Cu nanowires under a constant creep stress of  $0.56\sigma_y$ . To discern defects in the nanowires, colors are assigned to the atoms according to a local crystallinity classification visualized by common neighbor analysis. Perfect fcc atoms are removed for clarity; red represents hexagonal close-packed atoms, blue is body-centered cubic atoms, and green is for other atoms.

dislocation nucleation events, including nucleation of a leading partial dislocation on a slip plane intersecting with the first dislocation, nucleation of a twinning partial dislocation on a neighboring slip plane having the same Burgers vector as the leading dislocation, or the nucleation of a trailing partial dislocation on the same plane as the emitted dislocation.

If the creep stress is high, as illustrated in Figure 4b, the SF is then replaced by two twin boundaries (TBs), and the interaction of Shockley partial with surface atoms triggers a new SF. Stress-induced propagation of TBs and nucleation of new SFs lead to further elongation of the nanowire, as shown in Figure 4c. Eventually, necking and failure initiate at a strain of around 20%, as can be seen in Figure 4d.

In contrast, the deformation mechanisms of Pt under high creep stress ( $0.6\sigma_y$ ) are quite different, as shown in Figure 5 and

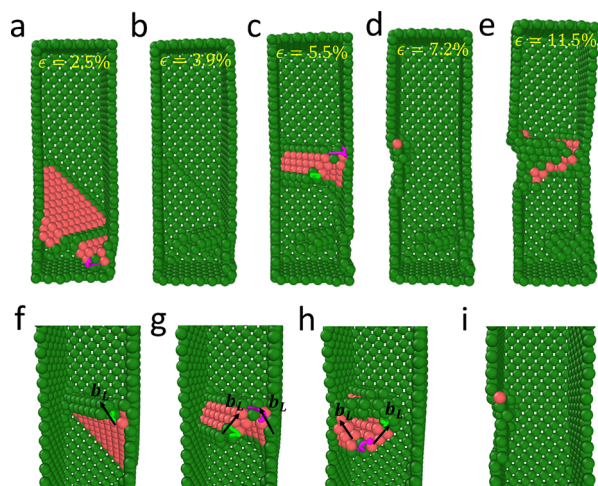


**Figure 5.** (a–e) Selected atomic configurations during the creep deformation of a Pt nanowire under a constant creep stress of  $0.6\sigma_y$ . (f–i) Direct observation of the L-C lock at 5.5% strain as in (c), which is formed by the interaction of two leading partial dislocations, where  $b_L$  marks the location of leading partials. To discern defects in the nanowires, colors are assigned to the atoms according to a local crystallinity classification by the dislocation extraction algorithm. Perfect fcc atoms are removed for clarity; red represents hexagonal close-packed atoms, blue is body-centered cubic atoms, and green is for other atoms. Two adjacent red planes, SF; green line,  $1/6[112]$  Shockley partial dislocation; purple line,  $1/6[110]$  stair-rod dislocation.

**Video S6.** Specifically, [Figure 5a](#) shows the yielding mechanism where a SF is nucleated from the bottom corner of the nanowire. Immediately after the nucleation of the first SF, a trailing partial is emitted on the same slip plane, resulting in a full dislocation and leaving a surface step on the surface of the nanowire, as illustrated in [Figure 5b](#). [Figure 5c,d](#) shows the formation of Lomer–Cottrell (L-C) locks with the detailed process illustrated in [Figure 5f,g](#). The L-C lock is formed by the interaction of two leading Shockley partial dislocations, which move under applied stress on two intersecting slip planes according to<sup>45</sup>

$$\frac{1}{6}[\bar{1}\bar{2}1] + \frac{1}{6}[2\bar{1}\bar{1}] \rightarrow \frac{1}{6}[1\bar{1}0] \quad (1)$$

The consequence of the reaction is the formation of a stair-rod  $\frac{1}{6}[1\bar{1}0]$  dislocation. [Figure 5f](#) shows the nucleation of the first leading partial from the right side of the image. When the leading partial reaches the opposite edge, another leading partial on a different  $\{111\}$  slip plane is triggered. When the two leading partials interact with each other, a stair-rod dislocation forms as marked by purple line in [Figure 5g](#). [Figure 5h](#) shows the formation of another L-C lock immediately after [Figure 5g](#). Eventually, the stair-rod dislocations propagate through the nanowire, leaving two parallel surface steps on the left surface of the nanowire, as shown in [Figure 5i](#), which is the enlarged snapshot corresponding to the configuration shown in [Figure 5d](#). Thus, in contrast to the partial dislocation-dominated deformation during high stress creep of Cu and Ag, the plasticity in the creep of Pt nanowires at high stress is dominated by full dislocations and L-C locks. This finding is consistent with recent *in situ* experiments on the constant strain rate deformation of ultrasmall Pt nanowires, which found full dislocations, and dislocation locks are the dominant mechanism

during the early deformation stage ( $\epsilon < 15\%$ ).<sup>46</sup> As the creep strain increases, necking occurs at around 12.5% tensile strain, which is caused by discrete cooperative slip events on different slip systems in the region where L-C locks exist, as can be seen in [Figure 5e](#).

**Superplasticity for Low Stresses and Long Time Scales.** The low stress ( $<0.45\sigma_y$ ) and long time scale ( $>10^{-5}$  s) creep behavior for Cu nanowires is illustrated in [Figure 6](#), which

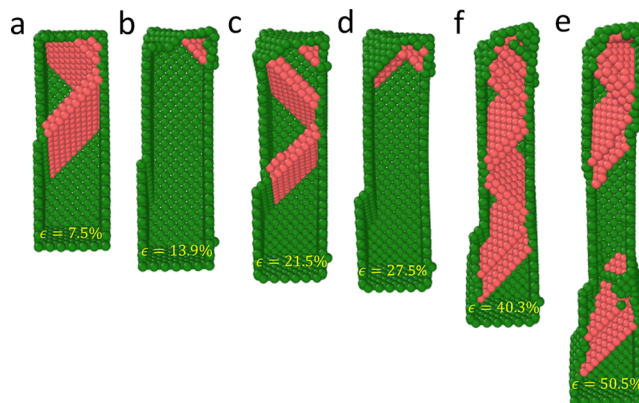


**Figure 6.** Selected atomic configurations during the creep deformation of the Cu nanowires under a constant stress of  $0.33\sigma_y$ . To discern defects in the nanowires, colors are assigned to the atoms according to a local crystallinity classification visualized by common neighbor analysis. Perfect fcc atoms are removed for clarity; red represents hexagonal close-packed atoms, blue is body-centered cubic atoms, and green is for other atoms.

corresponds to a creep stress of  $0.33\sigma_y$ , and where the full creep process can be seen in [Video S3](#). Similar to the high stress case, the secondary creep stage for low stresses starts with the nucleation of the first SF from a corner of the nanowire. When the first leading partial dislocation interacts with the nanowire surface, another SF is triggered on the intersecting slip plane, as can be seen in [Figure 6a](#). In contrast to formation of twin boundaries in [Figure 4](#), for low stresses, trailing partial dislocations are then observed on slip planes that contain SFs. The trailing partials glide through the slip planes, which eliminates the two SFs and forms full dislocations in conjunction with atomic-scale surface steps, leaving a defect-free nanocrystal, as illustrated in [Figure 6b](#). The surface step can serve as a dislocation nucleation source, and [Figure 6c](#) shows the emission of another sequential SF. Similar to what was observed in [Figure 6b](#), these SFs are then eliminated by the migration of trailing partial dislocations, as illustrated in [Figure 6d](#). A similar mechanism was also observed between [Figure 6d](#) and [Figure 6e](#), as seen in [Video S3](#), showing the importance of this dislocation behavior. As a result, the nanowire is able to exhibit substantial ductility and superplasticity with a prenecking strain of more than 50%, as can be seen in [Figure 6e](#).

A similar deformation mechanism is also observed for Ag nanowires, where the trailing partial-mediated deformation process leads to the superplasticity of the nanowire with prenecking strain of 60% at a stress of  $0.27\sigma_y$ , with snapshots of dislocation nucleation shown in [Figure S7](#) and with the full creep process shown in [Video S5](#). These are both in contrast to what is observed in Pt, where for a creep stress of  $0.37\sigma_y$ , the same full dislocation and L-C lock-dominated deformation are

observed with a prenecking strain of 16.5%, even though the creep time reaches 110 s, as seen in Figure S8 and Video S7.

The effect of the transition in deformation mechanism can also be observed by looking at the prenecking strain as a function of creep stress. Figure 7 shows that, for both Ag and

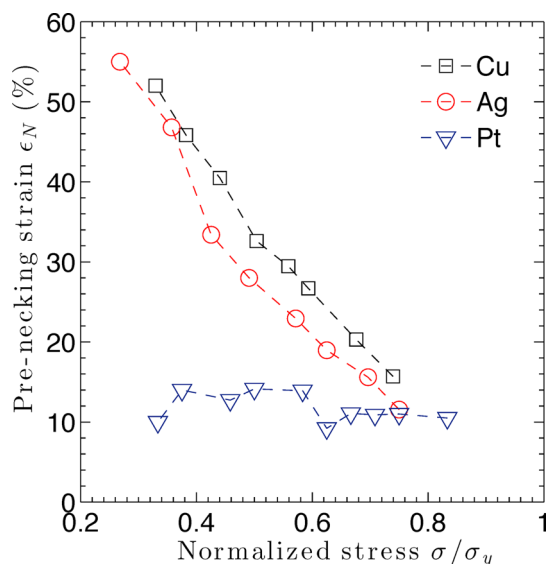


**Figure 7.** Elongation before necking as a function of normalized creep stress.

Cu, when the creep stress drops below about  $0.5\sigma_y$ , a substantial increment in prenecking strain is observed, which allows the nanowires to reach a superplastic elongation exceeding 50% before the onset of necking. In contrast, the prenecking strain does not appear to show much variation for Pt nanowires regardless of the creep stress.

The fact that superplasticity is not observed for Pt is due to the following two factors. First, both Ag and Cu have low SF energies,<sup>47</sup> and as such, the plastic deformation is governed by partial dislocations or twinning. In contrast, Pt has a very high SF energy, and thus full dislocations are typically observed, at least at the early stage ( $<15\%$ ) of plastic deformation.<sup>46</sup> For Ag

and Cu nanowires, when one leading partial dislocation sweeps across the nanowire cross section and reaches the surface, another leading partial dislocation is emitted on a different  $\{111\}$  slip system, which is intersecting with a previous slip plane, as illustrated in Figure 6. The successively formed SFs are then removed by the emission of trailing partials, which leads to the uniform elongation of the nanowire. Thus, we anticipate that superplasticity may be observed in other fcc metal nanowires that have SF energies similar to those of Cu and Ag for low creep stresses.

Furthermore, Pt nanocrystals can form dislocation locks, which will impede the dislocation motion, as shown both in Figure 5 and also recent experiments.<sup>46</sup> Figures 5 and S9 show direct observation of L-C locks in the SLME creep simulations of Pt nanowires for both high and low creep stresses. Dislocations tend to nucleate from the activated surface atoms where dislocation locks exist. When dislocations on different slip systems interact with each other, the dislocations are trapped by the L-C locks and the localized strain brings about the necking of the nanowire. As a result, the Pt nanowire starts to neck at a relatively small strain of around 15% regardless of the creep stress, with examples shown in Figures 5 and S9.

**Rate-Dependent Competition between Twinning and Trailing Partial Dislocations.** In addition to the atomistic observation of the governing creep mechanisms, we also performed a statistical examination of the mechanisms underpinning the transition to superplastic deformation at lower creep stresses for Ag and Cu nanowires. Specifically, Figure 8a summarizes the number of the three common partial dislocation types, including leading, trailing, and twinning partial dislocations, that are nucleated during secondary creep for Cu. These results were obtained by taking an average of five SLME simulations for each value of applied stress, in order to quantify the number and types of partial dislocations that occur prior to the onset of necking. The increasing number of trailing partials with decreasing stress as observed in Figure 8a is critical to enabling superplasticity because they remove SFs, as shown previously in Figure 6, which results in removal of internal planar defects and which enables the nanowire to nucleate additional partial dislocations. Continuation of this process

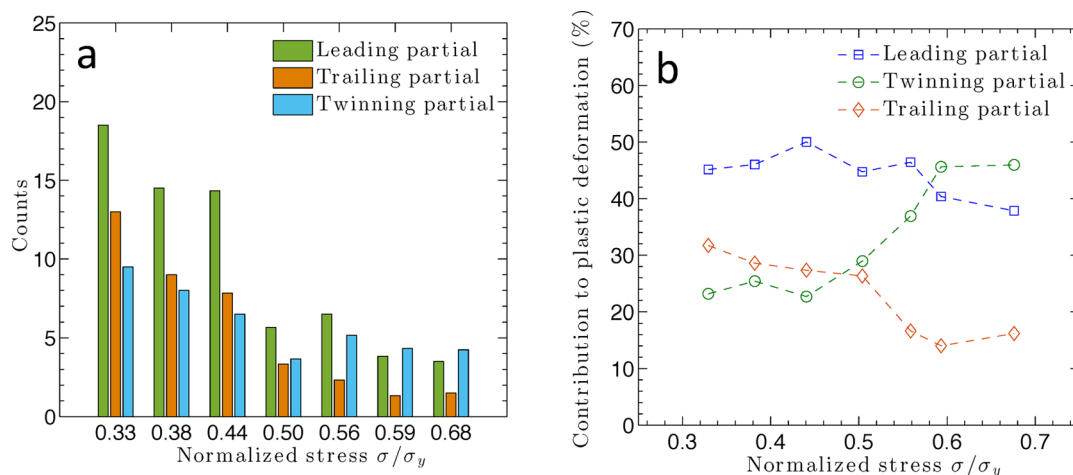


**Figure 8.** (a) Normalized creep stress dependence of the total number of three possible plastic deformation mechanisms: leading partials, trailing partials, and twinning partials formed during secondary creep prior to nanowire necking for Cu nanowires. (b) Normalized creep stress dependence for three partial dislocations and their contribution to the overall plastic strain during secondary creep prior to nanowire necking for Cu nanowires.

enables the generation of more total dislocations under low creep stresses than are observed at high applied stresses, as shown in Figure 8a.

We additionally investigated the competition between trailing and twinning partials, where Figure 8b shows the contribution from leading, trailing, and twinning partials to the total number of plastic events for Cu nanowires; Figure 8b represents the portion of each different partial dislocations under different stress levels, where, as can be seen, the plastic deformation can fit into two regions. In the high stress regime ( $0.5\text{--}0.7\sigma_y$ ), leading and twinning partials are the dominant mechanism during the creep process. However, the contribution from trailing partial dislocations starts to increase when the stress is reduced below  $0.45\sigma_y$ , which results in full dislocations gradually becoming as prevalent as and then preferred to twinning dislocations.

We further analyzed the activation energy for twinning and trailing partials under different applied stresses to help rationalize the observed transition from twinning dislocation-dominated creep in the high stress regime to trailing dislocation-mediated plasticity at lower stresses for Cu and Ag. This is important because twinning and slip occur on the same slip systems<sup>38,48</sup> and, as such, are in direct competition. Determining the activation energies for each will provide information on the rate dependence of each defect type for the different fcc metals we have considered. Following the procedure described by Jiang *et al.*,<sup>49</sup> a single SF was first introduced into a relaxed, defect-free nanowire using its known displacement fields. After that, a TB was generated by shearing the neighboring  $\{111\}$  plane in the  $\langle 112 \rangle$  direction, and full dislocation is formed by shearing the same  $\{111\}$  plane along the  $\langle 211 \rangle$  direction. Similar to the work of Zhu *et al.*,<sup>50</sup> the free-end nudged elastic band method was then utilized to determine the minimum energy path of the twinning and trailing partial dislocations under different external loads. The potential energy barrier  $Q_0(\sigma)$  was obtained based on the energy difference between the initial equilibrium state and the saddle point along the minimum energy pathway. The activation free energy at room temperature then can be calculated as  $Q(T,\sigma) = Q_0(\sigma)(1 - T/T_m)^{50}$  where  $T$  is the system temperature and  $T_m$  is the surface disordering temperature.

Figure 9 summarizes the stress-dependent activation energy for twinning and trailing partials as calculated at 300 K for Pt, Cu, and Ag. As can be seen, both Ag and Cu exhibit a crossover from twinning to trailing dislocation emission as the stress is decreased; the transition stress of about  $0.2\sigma_y$  for Cu is slightly larger than that of  $0.18\sigma_y$  for Ag. Furthermore, because the activation energy is lower in Ag than in Cu, we expect that the time scale at which the twinning to trailing transition occurs should be shorter than that for Cu. However, for Pt, the activation energy for trailing partials is always smaller than that of the twinning partial, which explains why only full dislocations are observed in the creep of Pt for all stresses we investigated.

The prediction of a transition stress of  $0.2\sigma_y$  for Cu is less than that seen in our SLME simulations, which predicts that more trailing partials will nucleate when the stress is under  $0.45\sigma_y$ . This is reasonable given that Figure 8 shows that a significant number of dislocations are nucleated during the creep process, whereas the activation energy analysis just discussed involves only a single defect in an otherwise pristine nanowire. We thus examined the effect of pre-existing defects on the activation energy if multiple partial dislocations are present in the nanowire. Figure S9 shows the process to

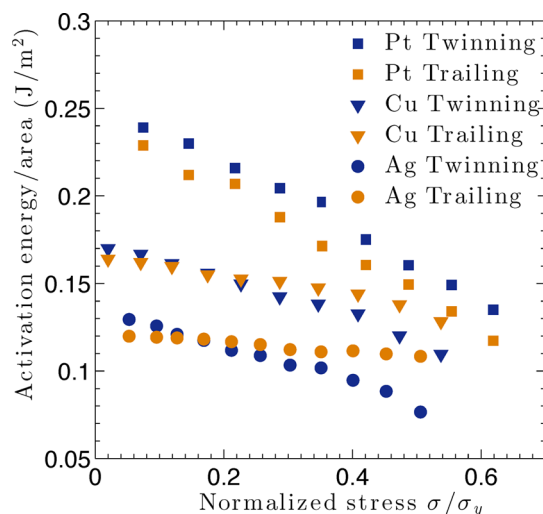


Figure 9. Activation energy for twinning and trailing partial dislocations as a function of external stress.

introduce an additional SF to the nanowire, whereas the activation energies of the twinning and trailing partials at different stresses for the Cu nanowire are summarized in Figure S10. Introducing the additional SF slightly lowers the activation energy of the trailing partial dislocation while having no obvious influence on the twinning partial. As a result, the transition stress increases to  $0.3\sigma_y$ , which is higher than  $0.2\sigma_y$  for single defect events.

We note that the transition stress of  $0.45\sigma_y$  seen in Figure 8 for Cu agrees well with the  $0.5\sigma_y$ , where the slope of the creep time *versus* stress curve changes (Figure 3). The reduction in the slope of the creep time *versus* stress plot in Figure 3 after the transition to trailing partials is also qualitatively reasonable because the slope of the activation energy barrier for trailing partials is smaller than that of the twinning partial for Ag and Cu nanowires, as shown in Figure 9. However, for Pt nanowires, the curve does not show a transition in its slope, which is consistent with the observation of full dislocations being the dominant deformation mechanism at all stress levels we investigated.

These results also demonstrate that the rate dependence of the different competitive defect processes, such as twinning and trailing partials, governs the transition to superplasticity for the lower creep stresses we have observed in Cu and Ag nanowires, as well as the creep time transition. These coincide with the theoretical results of Warner *et al.*,<sup>38</sup> who found that a twinning to slip transition in fcc metals related to defect nucleation from a crack tip was on the order of microseconds or longer. However, we note that we do not expect complete or even quantitative agreement with the predictions of Warner *et al.*<sup>38</sup> For example, they predicted that twinning would be observed in Pt at high stresses, which is not observed in our simulations. This is because their model assumed defect nucleation from a pre-existing crack tip, whereas our simulations were performed investigating creep of single-crystal nanowires without a similar sharp discontinuity. Overall, our simulations demonstrate the importance of capturing longer time scales in order to observe rate-dependent defect transitions.

Superplastic behavior has been reported in other studies that have examined the deformation of metal nanowires. For example, in the experimental works by Seo *et al.*,<sup>51,52</sup> failure strains of about 50% were observed through the tensile stress-

driven reorientation of rhombic fcc metal  $\langle 110 \rangle / \{ 111 \}$  nanowires to a  $\langle 100 \rangle / \{ 100 \}$  orientation. In more recent work by Zhong *et al.*,<sup>24</sup> room temperature superplasticity was observed in Ag nanocrystals with diameters ranging from 15 to 80 nm. There, the superplasticity was enabled by a slip-activated surface creep mechanism, whereby surface-step diffusion was effective in suppressing localized plasticity and necking that limits the tensile ductility of the material. Surface-step diffusion is not observed in our simulations despite the small cross sectional sizes because our nanowires had uniform cross sections along the loading direction. In contrast, the surface diffusion in the work of Zhong *et al.*<sup>24</sup> was driven by a gradient in nanowire radius, where the chemical potential difference along the surface drove the migration of surface steps from the center to the ends of the nanowire along the length direction. Therefore, the mechanism underlying the superplasticity observed in our study, for example, that of a rate-dependent plasticity transition that manifests itself at lower applied stresses and longer time scales, is different from previously reported ones.

## CONCLUSIONS

We have utilized atomistic simulations that can access experimentally relevant time scales to investigate the creep deformation of single-crystal fcc metal nanowires. Superplastic creep at low creep stresses for some metals (Ag, Cu) is observed, which is driven by a rate-dependent transition from twinning to trailing partial dislocations at micro- and millisecond time scales and which results in tensile strains reaching 50% prior to necking and failure at low creep stresses ( $< 0.5\sigma_y$ ). The plasticity transition is captured because the time scales accessed by the SLME method correspond to those at which rate dependence controls the type of planar defect that is nucleated. Overall, this work demonstrates the importance of rate-dependent mechanical processes on the time-dependent mechanical behavior and properties of nanomaterials.

## METHODS

To study the creep mechanisms of single-crystal fcc metal nanowires, we use the recently developed SLME method<sup>26,36,37,39,40,53,54</sup> to overcome the high strain rate and short time scale computational hurdles that are intrinsic to classical MD. The SLME approach performs potential energy surface exploration using a modified and more computationally efficient version of the autonomous basin climbing method originally proposed by Yip and co-workers.<sup>55–57</sup> We note that the SLME method has recently been applied to study creep in amorphous solids<sup>58</sup> and also strain-rate-dependent plasticity and failure transitions in bicrystalline metal nanowires.<sup>26</sup>

We consider single-crystal  $\langle 100 \rangle / \{ 100 \}$  Cu, Ag, and Pt nanowires. We chose these three fcc metals because they have been predicted to undergo a plasticity transition from twinning to full dislocation formation at different times in the study of crack-tip behavior at different stress levels.<sup>38</sup> We will examine and focus on this potential deformation mechanism transition through our creep simulations. We chose single-crystal nanowires due to their relative simplicity, as we do not expect to observe the classical grain-boundary-mediated mechanisms for creep that are seen in polycrystalline metals.<sup>27,28</sup>

The nanowires were simulated with different embedded atom method potentials, that is, by Mishin *et al.* for Cu,<sup>59</sup> Wu and Trinkle potential for Ag,<sup>60</sup> and Sheng *et al.* potential for Pt.<sup>61</sup> Due to the computational expense of the SLME method, all nanowires in our SLME simulations have a square cross section with width of about 2.5 nm and aspect ratio of 3. We also verified that the results we present are independent of nanowire length, by performing SLME simulations with periodic boundary conditions along the nanowire length direction

to mimic infinitely long nanowires. Free boundary conditions were applied along all three directions of the nanowire. The energy of the nanowires was first minimized using the conjugate-gradient method, after which they were relaxed for 20 ps at 300 K in the canonical (NVT) ensemble. A constant uniaxial tensile stress to induce creep was then applied along the axial direction at one end of the nanowire, and the other end was held fixed; there was no constraint in the transverse directions. All simulations were performed using the publicly available simulation code LAMMPS,<sup>62</sup> whereas the OVITO package<sup>63</sup> was used for visualization. Further details about the SLME procedure and methodology can be found in the [Supporting Information](#).

## ASSOCIATED CONTENT

### Supporting Information

The Supporting Information is available free of charge on the ACS Publications website at DOI: [10.1021/acsnano.8b02199](https://doi.org/10.1021/acsnano.8b02199).

Video S1 shows the creep deformation of a Cu nanowire using MD for a creep stress of  $0.59\sigma_y$  at room temperature (AVI)

Video S2 shows the creep mechanism of a Cu nanowire using SLME for a creep stress of  $0.59\sigma_y$  at room temperature (AVI)

Video S3 shows the creep mechanism of a Cu nanowire using SLME for a creep stress of  $0.33\sigma_y$  at room temperature (AVI)

Video S4 shows the creep mechanism of a Ag nanowire using SLME for a creep stress of  $0.62\sigma_y$  at room temperature (AVI)

Video S5 shows the creep mechanism of a Ag nanowire using SLME for a creep stress of  $0.27\sigma_y$  at room temperature (AVI)

Video S6 shows the creep mechanism of a Pt nanowire using SLME for a creep stress of  $0.6\sigma_y$  at room temperature (AVI)

Video S7 shows the creep mechanism of a Pt nanowire using SLME for a creep stress of  $0.37\sigma_y$  at room temperature (AVI)

Deformation processes of the nanowires as obtained using the SLME method; benchmarking of the SLME method against MD simulations at high stresses, in addition to the creep curves and deformation mechanisms for Ag and Pt nanowires at different creep stress levels; activation energy calculation for configurations with multiple SFs (PDF)

## AUTHOR INFORMATION

### Corresponding Author

\*E-mail: [parkhs@bu.edu](mailto:parkhs@bu.edu).

### ORCID

Harold S. Park: [0000-0001-5365-7776](https://orcid.org/0000-0001-5365-7776)

### Notes

The authors declare no competing financial interest.

## ACKNOWLEDGMENTS

H.S.P. and W.T. gratefully acknowledge the support of the Mechanical Engineering department at Boston University. P.C. acknowledges financial support from the U.S. Department of Energy under Grant No. DE-NE0008450.

## REFERENCES

(1) Langley, D.; Giusti, G.; Mayousse, C.; Celle, C.; Bellet, D.; Simonato, J.-P. Flexible Transparent Conductive Materials Based on

Silver Nanowire Networks: A Review. *Nanotechnology* **2013**, *24*, 452001.

(2) Bernal, R. A.; Filleter, T.; Connell, J. G.; Sohn, K.; Huang, J.; Lahun, L. J.; Espinosa, H. D. In Situ Electron Microscopy Four-Point Electromechanical Characterization of Freestanding Metallic and Semiconducting Nanowires. *Small* **2014**, *10*, 725–733.

(3) Li, X.; Dao, M.; Eberl, C.; Hodge, A. M.; Gao, H. Fracture, Fatigue, and Creep of Nanotwinned Metals. *MRS Bull.* **2016**, *41*, 298–304.

(4) Ramachandramoorthy, R.; Wang, Y.; Aghaei, A.; Richter, G.; Cai, W.; Espinosa, H. D. Reliability of Single Crystal Silver Nanowire-Based Systems: Stress Assisted Instabilities. *ACS Nano* **2017**, *11*, 4768–4776.

(5) Zhu, Y.; Xu, F. Buckling of Aligned Carbon Nanotubes as Stretchable Conductors: A New Manufacturing Strategy. *Adv. Mater.* **2012**, *24*, 1073–1077.

(6) Yao, S.; Zhu, Y. Nanomaterial-Enabled Stretchable Conductors: Strategies, Materials and Devices. *Adv. Mater.* **2015**, *27*, 1480–1511.

(7) Xu, F.; Zhu, Y. Highly Conductive and Stretchable Silver Nanowire Conductors. *Adv. Mater.* **2012**, *24*, 5117–5122.

(8) Greer, J. R.; Oliver, W. C.; Nix, W. D. Size Dependence of Mechanical Properties of Gold at the Micron Scale in the Absence of Strain Gradients. *Acta Mater.* **2005**, *53*, 1821–1830.

(9) Greer, J. R.; Nix, W. D. Nanoscale Gold Pillars Strengthened Through Dislocation Starvation. *Phys. Rev. B: Condens. Matter Mater. Phys.* **2006**, *73*, 245410.

(10) Uchic, M. D.; Dimiduk, D. M.; Florando, J. N.; Nix, W. D. Sample Dimensions Influence Strength and Crystal Plasticity. *Science* **2004**, *305*, 986–989.

(11) Han, X.; Zheng, K.; Zhang, Y.; Zhang, X.; Zhang, Z.; Wang, Z. L. Low-Temperature In Situ Large-Strain Plasticity of Silicon Nanowires. *Adv. Mater.* **2007**, *19*, 2112–2118.

(12) Yue, Y.; Liu, P.; Zhang, Z.; Han, X.; Ma, E. Approaching the Theoretical Elastic Strain Limit in Copper Nanowires. *Nano Lett.* **2011**, *11*, 3151–3155.

(13) Yue, Y.; Liu, P.; Deng, Q.; Ma, E.; Zhang, Z.; Han, X. Quantitative Evidence of Crossover Toward Partial Dislocation Mediated Plasticity in Copper Single Crystalline Nanowires. *Nano Lett.* **2012**, *12*, 4045–4049.

(14) Zhu, Y. Mechanics of Crystalline Nanowires: An Experimental Perspective. *Appl. Mech. Rev.* **2017**, *69*, 010802.

(15) Park, H. S.; Cai, W.; Espinosa, H. D.; Huang, H. Mechanics of Crystalline Nanowires. *MRS Bull.* **2009**, *34*, 178–183.

(16) Weinberger, C. R.; Cai, W. Plasticity of Metal Nano Wires. *J. Mater. Chem.* **2012**, *22*, 3277–3292.

(17) Narayanan, S.; Cheng, G.; Zeng, Z.; Zhu, Y.; Zhu, T. Strain Hardening and Size Effect in Five-Fold Twinned Ag Nanowires. *Nano Lett.* **2015**, *15*, 4037–4044.

(18) Zhu, Y.; Qin, Q.; Xu, F.; Fan, F.; Ding, Y.; Zhang, T.; Wiley, B. J.; Wang, Z. L. Size Effects on Elasticity, Yielding, and Fracture of Silver Nano Wires: In Situ Experiments. *Phys. Rev. B: Condens. Matter Mater. Phys.* **2012**, *85*, 045443.

(19) Greer, J. R.; De Hosson, J. T. M. Plasticity in Small-Sized Metallic Systems: Intrinsic Versus Extrinsic Size Effect. *Prog. Mater. Sci.* **2011**, *56*, 654–724.

(20) Cheng, G.; Miao, C.; Qin, Q.; Li, J.; Xu, F.; Haftbaradaran, H.; Dickey, E. C.; Gao, H.; Zhu, Y. Large Anelasticity and Associated Energy Dissipation in Single-Crystalline Nanowires. *Nat. Nanotechnol.* **2015**, *10*, 687–691.

(21) Qin, Q.; Yin, S.; Cheng, G.; Li, X.; Chang, T.-H.; Richter, G.; Zhu, Y.; Gao, H. Recoverable Plasticity in Penta-Twinned Metallic Nanowires Governed by Dislocation Nucleation and Retraction. *Nat. Commun.* **2015**, *6*, 5983.

(22) Zhong, L.; Sansoz, F.; He, Y.; Wang, C.; Zhang, Z.; Mao, S. X. Slip-Activated Surface Creep with Room-Temperature Super-Elongation in Metallic Nanocrystals. *Nat. Mater.* **2017**, *16*, 439–445.

(23) Chen, B.; Gao, Q.; Wang, Y.; Liao, X.; Mai, Y.-W.; Tan, H. H.; Zou, J.; Ringer, S. P.; Jagadish, C. Anelastic Behavior in GaAs Semiconductor Nanowires. *Nano Lett.* **2013**, *13*, 3169–3172.

(24) Zhong, L.; Sansoz, F.; He, Y.; Wang, C.; Zhang, Z.; Mao, S. X. Slip-Activated Surface Creep with Room-Temperature Super-Elongation in Metallic Nanocrystals. *Nat. Mater.* **2017**, *16*, 439–445.

(25) Sun, J.; He, L.; Lo, Y.-C.; Xu, T.; Bi, H.; Sun, L.; Zhang, Z.; Mao, S. X.; Li, J. Liquid-Like Pseudoelasticity of Sub-10-nm Crystalline Silver Particles. *Nat. Mater.* **2014**, *13*, 1007–1012.

(26) Tao, W.; Cao, P.; Park, H. S. Atomistic Simulation of the Rate-Dependent Ductile-to-Brittle Failure Transition in Bicrystalline Metal Nanowires. *Nano Lett.* **2018**, *18*, 1296–1304.

(27) Nabarro, F. Creep in Commercially Pure Metals. *Acta Mater.* **2006**, *54*, 263–295.

(28) Meyers, M. A.; Mishra, A.; Benson, D. J. Mechanical Properties of Nanocrystalline Materials. *Prog. Mater. Sci.* **2006**, *51*, 427–556.

(29) Huang, P.; Wang, F.; Xu, M.; Xu, K.; Lu, T. Dependence of Strain Rate Sensitivity upon Deformed Microstructures in Nanocrystalline Cu. *Acta Mater.* **2010**, *58*, 5196–5205.

(30) Darling, K.; Rajagopalan, M.; Komarasamy, M.; Bhatia, M.; Hornbuckle, B.; Mishra, R.; Solanki, K. Extreme Creep Resistance in a Microstructurally Stable Nanocrystalline Alloy. *Nature* **2016**, *537*, 378–381.

(31) Yamakov, V.; Wolf, D.; Phillpot, S.; Mukherjee, A.; Gleiter, H. Deformation-Mechanism Map for Nanocrystalline Metals by Molecular-Dynamics Simulation. *Nat. Mater.* **2004**, *3*, 43.

(32) Wolf, D.; Yamakov, V.; Phillpot, S.; Mukherjee, A.; Gleiter, H. Deformation of Nanocrystalline Materials by Molecular-Dynamics Simulation: Relationship to Experiments? *Acta Mater.* **2005**, *53*, 1–40.

(33) Wang, Y.-J.; Ishii, A.; Ogata, S. Transition of Creep Mechanism in Nanocrystalline Metals. *Phys. Rev. B: Condens. Matter Mater. Phys.* **2011**, *84*, 224102.

(34) Jiao, S.; Kulkarni, Y. Molecular Dynamics Study of Creep Mechanisms in Nanotwinned Metals. *Comput. Mater. Sci.* **2015**, *110*, 254–260.

(35) Lau, T. T.; Kushima, A.; Yip, S. Atomistic Simulation of Creep in a Nanocrystal. *Phys. Rev. Lett.* **2010**, *104*, 175501.

(36) Yan, X.; Cao, P.; Tao, W.; Sharma, P.; Park, H. S. Atomistic Modeling at Experimental Strain Rates and Time Scales. *J. Phys. D: Appl. Phys.* **2016**, *49*, 493002.

(37) Fan, Y.; Osetskii, Y. N.; Yip, S.; Yildiz, B. Mapping Strain Rate Dependence of Dislocation-Defect Interactions by Atomistic Simulations. *Proc. Natl. Acad. Sci. U. S. A.* **2013**, *110*, 17756–17761.

(38) Warner, D.; Curtin, W.; Qu, S. Rate Dependence of Crack-Tip Processes Predicts Twinning Trends in FCC Metals. *Nat. Mater.* **2007**, *6*, 876.

(39) Cao, P.; Li, M.; Heugle, R. J.; Park, H. S.; Lin, X. A Self-Learning Metabasin Escape Algorithm and the Metabasin Correlation Length of Supercooled Liquids. *Phys. Rev. E* **2012**, *86*, 016710.

(40) Cao, P.; Park, H. S.; Lin, X. Strain-rate and Temperature-Driven Transition in the Shear Transformation Zone for Two-Dimensional Amorphous Solids. *Phys. Rev. E* **2013**, *88*, 042404.

(41) Nie, K.; Wu, W.-P.; Zhang, X.-L.; Yang, S.-M. Molecular Dynamics Study on the Grain Size, Temperature, and Stress Dependence of Creep Behavior in Nanocrystalline Nickel. *J. Mater. Sci.* **2017**, *52*, 2180–2191.

(42) Peng, C.; Zhong, Y.; Lu, Y.; Narayanan, S.; Zhu, T.; Lou, J. Strain Rate Dependent Mechanical Properties in Single Crystal Nickel Nanowires. *Appl. Phys. Lett.* **2013**, *102*, 083102.

(43) Mukherjee, A. K.; Bird, J. E.; Dorn, J. E. Experimental Correlations for High-Temperature Creep. Report UCRL-18526; CONF-681018-2, University of California, Berkeley, 1968.

(44) Wilshire, B.; Battenbough, A. Creep and Creep Fracture of Polycrystalline Copper. *Mater. Sci. Eng., A* **2007**, *443*, 156–166.

(45) Hull, D.; Bacon, D. J. *Introduction to Dislocations*; Elsevier, 2011; Vol. 37.

(46) Wang, L.; Teng, J.; Sha, X.; Zou, J.; Zhang, Z.; Han, X. Plastic Deformation Through Dislocation Saturation in Ultrasmall Pt Nanocrystals and Its In Situ Atomistic Mechanisms. *Nano Lett.* **2017**, *17*, 4733–4739.

(47) Li, B.; Sui, M.; Mao, S. Twinability Prediction for FCC Metals. *J. Mater. Sci. Technol.* **2011**, *27*, 97–100.

- (48) Park, H. S.; Gall, K.; Zimmerman, J. A. Deformation of FCC Nanowires by Twinning and Slip. *J. Mech. Phys. Solids* **2006**, *54*, 1862–1881.
- (49) Jiang, J.-W.; Leach, A. M.; Gall, K.; Park, H. S.; Rabczuk, T. A Surface Stacking Fault Energy Approach to Predicting Defect Nucleation in Surface-Dominated Nanostructures. *J. Mech. Phys. Solids* **2013**, *61*, 1915–1934.
- (50) Zhu, T.; Li, J.; Samanta, A.; Leach, A.; Gall, K. Temperature and Strain-Rate Dependence of Surface Dislocation Nucleation. *Phys. Rev. Lett.* **2008**, *100*, 025502.
- (51) Seo, J.-H.; Yoo, Y.; Park, N.-Y.; Yoon, S.-W.; Lee, H.; Han, S.; Lee, S.-W.; Seong, T.-Y.; Lee, S.-C.; Lee, K.-B.; Cha, P.-R.; Park, H. S.; Kim, B.; Ahn, J.-P. Superplastic Deformation of Defect-Free Au Nanowires by Coherent Twin Propagation. *Nano Lett.* **2011**, *11*, 3499–3502.
- (52) Seo, J.-H.; Park, H. S.; Yoo, Y.; Seong, T.-Y.; Li, J.; Ahn, J.-P.; Kim, B.; Choi, I.-S. Origin of Size Dependency in Coherent-Twin Propagation-Mediated Tensile Deformation of Noble Metal Nanowires. *Nano Lett.* **2013**, *13*, 5112–5116.
- (53) Cao, P.; Lin, X.; Park, H. S. Strain-Rate and Temperature Dependence of Yield Stress of Amorphous Solids via a Self-Learning Metabasin Escape Algorithm. *J. Mech. Phys. Solids* **2014**, *68*, 239–250.
- (54) Yan, X.; Sharma, P. Time-Scaling in Atomistics and the Rate-Dependent Mechanical Behavior of Nanostructures. *Nano Lett.* **2016**, *16*, 3487–3492.
- (55) Kushima, A.; Lin, X.; Li, J.; Eapen, J.; Mauro, J. C.; Qian, X.; Diep, P.; Yip, S. Computing the Viscosity of Supercooled Liquids. *J. Chem. Phys.* **2009**, *130*, 224504.
- (56) Fan, Y.; Osetskiy, Y. N.; Yip, S.; Yildiz, B. Mapping Strain Rate Dependence of Dislocation-Defect Interactions by Atomistic Simulations. *Proc. Natl. Acad. Sci. U. S. A.* **2013**, *110*, 17756–17761.
- (57) Fan, Y.; Kushima, A.; Yip, S.; Yildiz, B. Mechanism of Void Nucleation and Growth in Bcc Fe: Atomistic Simulations at Experimental Time Scales. *Phys. Rev. Lett.* **2011**, *106*, 125501.
- (58) Cao, P.; Short, M. P.; Yip, S. Understanding the Mechanisms of Amorphous Creep Through Molecular Simulation. *Proc. Natl. Acad. Sci. U. S. A.* **2017**, *114*, 13631–13636.
- (59) Mishin, Y.; Mehl, M.; Papaconstantopoulos, D.; Voter, A.; Kress, J. Structural Stability and Lattice Defects in Copper: Ab Initio, Tight-Binding, and Embedded-Atom Calculations. *Phys. Rev. B: Condens. Matter Mater. Phys.* **2001**, *63*, 224106.
- (60) Wu, H. H.; Trinkle, D. R. Cu/Ag Eam Potential Optimized for Heteroepitaxial Diffusion from Ab Initio Data. *Comput. Mater. Sci.* **2009**, *47*, 577–583.
- (61) Sheng, H.; Kramer, M.; Cadien, A.; Fujita, T.; Chen, M. Highly Optimized Embedded-Atom-Method Potentials for Fourteen FCC Metals. *Phys. Rev. B: Condens. Matter Mater. Phys.* **2011**, *83*, 134118.
- (62) Plimpton, S. Fast Parallel Algorithms for Short-Range Molecular Dynamics. *J. Comput. Phys.* **1995**, *117*, 1–19.
- (63) Stukowski, A. Visualization and Analysis of Atomistic Simulation Data with OVITO—the Open Visualization Tool. *Modell. Simul. Mater. Sci. Eng.* **2010**, *18*, 015012.